

Ising superconductivity induced from valley symmetry breaking in twisted trilayer graphene

J. González¹ and T. Stauber^{2,3}

¹ Instituto de Estructura de la Materia, CSIC, E-28006 Madrid, Spain

² Materials Science Factory, Instituto de Ciencia de Materiales de Madrid, CSIC, E-28049 Madrid, Spain

³ Theoretical Physics III, Center for Electronic Correlations and Magnetism, Institute of Physics, University of Augsburg, D-86135 Augsburg, Germany

(Dated: March 17, 2022)

We show that the e - e interaction induces a strong breakdown of valley symmetry in twisted trilayer graphene, leading to a state where the two spin projections have opposite sign of the valley symmetry breaking order parameter. This leads to a spin-valley locking which has important implications for the superconductivity, explaining its protection against magnetic fields. The effect of valley symmetry breaking is validated as it reproduces the experimental observation of the reset of the Hall density at 2-hole doping. It also implies a reduction of the symmetry of the bands from C_6 to C_3 , with an enhancement of the anisotropy of the Fermi lines which is at the origin of a Kohn-Luttinger (pairing) instability. The isotropy of the bands is gradually recovered, however, when the Fermi level approaches the bottom of the second valence band, explaining why the superconductivity is lost when doping beyond 3 holes per moiré unit cell in twisted trilayer graphene.

Introduction.— The discovery of superconductivity and its parent insulating phases at the magic angle of twisted bilayer graphene (TBG)^{1,2} has opened a new era in the investigation of strongly correlated phenomena in two-dimensional electron systems. There is an ongoing debate about the origin of the superconductivity in TBG^{3–41}, which could also clarify whether a similar phenomenon can arise in other moiré van der Waals materials. In this regard, superconductivity has been already observed in twisted trilayer graphene (TTG),^{42,43} showing unconventional features like reentrant behavior under large magnetic fields.^{44–50} Moreover, in the presence of spin-orbit coupling, a valley symmetry (VS) broken state can lead to a zero-field superconducting diode effect.^{51,52}

TTG has also shown a striking phenomenon of reset of the Hall density at integer fillings of the lowest valence and conduction bands.^{42,43} Specifically at 2-hole doping, it has been found that the Hall density jumps from a divergent value down to zero. This observation is particularly important, since the effect of reset precedes the development of the superconducting regime right below 2-hole doping (as well as right above 2-electron doping in the conduction band).

In this paper, we show that the extended Coulomb interaction has a natural tendency to induce the breakdown of the VS of TTG, which lifts the degeneracy of the Dirac cones by moving them up and down in energy, respectively. This effect becomes strongest at 2-hole doping, such that the Fermi level is pushed up to the vertices of the Dirac cones in the lower valley. At that filling, the Dirac nodes turn out to be unstable against time-reversal symmetry breaking with condensation of a Haldane mass, opening a gap at the Fermi level. As we show below, this is the mechanism responsible for the experimentally observed reset of the Hall density.

We apply a self-consistent Hartree-Fock resolution in real space, which reveals the existence of a state where

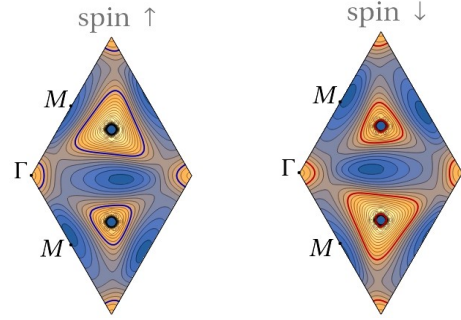


FIG. 1. Energy contour maps showing the Fermi lines in the second valence band for spin-up (a) and spin-down electrons (b) in the moiré Brillouin zone of twisted trilayer graphene with twist angle of $\approx 1.61^\circ$, for dielectric constant $\epsilon = 48$ and filling fraction of 2.4 holes per moiré unit cell.

the two spin projections have opposite sign of the VS breaking order parameter. The dispersions for spin-up and spin-down electrons are then symmetric upon exchange of the two K points in the Brillouin zone, as seen in Fig. 1, in such a way that the two spin projections are preferentially attached to opposite K points. This effect of spin-valley locking implies that the superconductivity must be of Ising type^{53–55} in TTG. The splitting of the bands for spin up and spin down around each K point means that there is in general an energy cost to invert one of the spin projections. We will see that this explains the protection of the superconductivity against unusually large magnetic fields, as observed experimentally.

The breakdown of VS leads also to a reduction of the symmetry of the bands from C_6 to C_3 , as the latter is the symmetry enforced in a single valley. This enhanced anisotropy induces a strong modulation of the e - e scattering, which is the seed needed in order to induce a Kohn-Luttinger (pairing) instability, driven solely by electron interactions^{56,57}. The instability is here amplified by the

screening from a large number of electron-hole excitations across the very regular triangular Fermi lines shown in Fig. 1, leading to an effective attractive interaction in the channel corresponding to the $\cos(3\phi)$ harmonic. This mechanism of attraction is lost, however, for doping levels beyond filling fraction $\nu \approx -3$ as the geometry of the Fermi line changes into elliptic form (as seen around the M points in the plot of Fig. 2), explaining the limited range of superconductivity in the hole-doped regime of TTG.

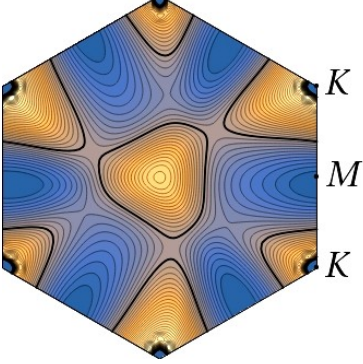


FIG. 2. Energy contour map of the second valence band in the Brillouin zone of TTG at twist angle $\theta \approx 1.61^\circ$, computed in a self-consistent Hartree-Fock approximation with dielectric constant $\epsilon = 48$ and filling fraction of 2.8 holes per moiré unit cell. The thick contour stands for the Fermi line. Contiguous contour lines differ by a constant step of 0.4 meV, from lower energies in blue to higher energies in light color.

Valley symmetry breaking.— We deal with the setup of TTG usually realized in the experiments, in which the two outer layers are rotated by the same angle θ with respect to the central layer. We model this configuration by taking a twist angle $\theta \approx 1.61^\circ$ belonging to the set of commensurate superlattices realized by TBG. Then, the low-energy states are distributed into a Dirac-like band, with states even under mirror symmetry with respect to the central plane, and two additional valence and conduction bands, with states odd under the mirror symmetry (see the Supplemental Material (SM)⁵⁸). The latter are the counterpart of the lowest-energy bands of TBG, and they become progressively flatter when approaching the magic angle of TTG, which is $\approx 1.6^\circ$.

In what follows, we apply an atomistic approach to TTG, based on a tight-binding model for the π orbitals of the carbon atoms. The Hamiltonian H is written as

$$H = H_0 + H_{\text{int}} , \quad (1)$$

where H_0 stands for the non-interacting tight-binding Hamiltonian and H_{int} is the interaction part. This is expressed in terms of creation (annihilation) operators $a_{i\sigma}^\dagger$ ($a_{i\sigma}$) for electrons at each carbon site i with spin σ

$$H_{\text{int}} = \frac{1}{2} \sum_{i,j,\sigma,\sigma'} a_{i\sigma}^\dagger a_{i\sigma} v_{\sigma\sigma'}(\mathbf{r}_i - \mathbf{r}_j) a_{j\sigma'}^\dagger a_{j\sigma'} , \quad (2)$$

We take $v_{\sigma\sigma'}$ as the extended Coulomb potential, with the long-range tail cut off at a distance dictated by the screening length ξ , arising from the presence of nearby metallic gates, and with the strength further reduced by a dielectric constant ϵ (see the SM for all the details).

We resort to a self-consistent Hartree-Fock approximation in order to study the effects of the e - e interaction. In this approach, the full electron propagator G is represented in terms of a set of eigenvalues $\varepsilon_{a\sigma}$ and eigenvectors $\phi_{a\sigma}(\mathbf{r}_i)$ modified by the interaction, in such a way that in the static limit

$$(G)_{i\sigma,j\sigma} = - \sum_a \frac{1}{\varepsilon_{a\sigma}} \phi_{a\sigma}(\mathbf{r}_i) \phi_{a\sigma}(\mathbf{r}_j)^* . \quad (3)$$

In the Hartree-Fock approximation, the electron self-energy Σ can be also expressed entirely in terms of the set of $\phi_{a\sigma}(\mathbf{r}_i)$. In the static limit, we have

$$(\Sigma)_{i\sigma,j\sigma} = 2\mathbb{I}_{ij} \sum_a' \sum_{l,\sigma'} v_{\sigma\sigma'}(\mathbf{r}_i - \mathbf{r}_l) |\phi_{a\sigma'}(\mathbf{r}_l)|^2 - v_{\sigma\sigma}(\mathbf{r}_i - \mathbf{r}_j) \sum_a' \phi_{a\sigma}(\mathbf{r}_i) \phi_{a\sigma}(\mathbf{r}_j)^* , \quad (4)$$

where the prime means that the sum is to be carried over the occupied levels⁵⁹.

Our Hartree-Fock approach consists then in performing a self-consistent resolution when the electron propagator is corrected by the self-energy (4). The Fock contribution to the self-energy (4) becomes essential in order to account for the dynamical symmetry breaking. In TTG, we find that the dominant patterns correspond to the breakdown of time-reversal invariance⁵⁸. This may be characterized by two different order parameters

$$P_{\pm}^{(\sigma)} = \text{Im} \left(\sum_{i \in A} \left(h_{i_1 i_2}^{(\sigma)} h_{i_2 i_3}^{(\sigma)} h_{i_3 i_1}^{(\sigma)} \right)^{\frac{1}{3}} \pm \sum_{i \in B} \left(h_{i_1 i_2}^{(\sigma)} h_{i_2 i_3}^{(\sigma)} h_{i_3 i_1}^{(\sigma)} \right)^{\frac{1}{3}} \right) \quad (5)$$

where the sums run over the loops made of three nearest neighbors i_1, i_2 and i_3 of each atom i in graphene sublattices A and B , with matrix elements

$$h_{ij}^{(\sigma)} = \sum_a' \phi_{a\sigma}(\mathbf{r}_i) \phi_{a\sigma}(\mathbf{r}_j)^* . \quad (6)$$

One can check that $P_{-}^{(\sigma)}$ gives a measure of the mismatch in the energy shift of the bands in the two valleys of the electron system. On the other hand, a nonvanishing $P_{+}^{(\sigma)}$ is the hallmark of a Chern insulating phase, as described originally by Haldane⁶⁰.

The analysis of internal screening in TTG reveals that the effective value of the dielectric constant corresponds in our model to $\epsilon \sim 50$ (see SM⁵⁸). The extended Coulomb interaction is then in a regime where the dominant order parameter is that of VS breaking, while the pattern associated to $P_{+}^{(\sigma)}$ has a subdominant character⁵⁸. This can be seen in Fig. 3, which shows

the splitting at the K point of the two upper Dirac cones from the two valleys, as an effect of VS breaking. At 2-hole doping, the Fermi level should be then at the vertex of the Dirac cone of the lower valley. However, the interaction proves to be strong enough to trigger the condensation of the Haldane mass, which leads to the gap seen in Fig. 3 at the Fermi level. In this discussion, the effect of the “third”, lowest Dirac cone can be safely neglected as this band belongs to a different representation of the mirror symmetry.

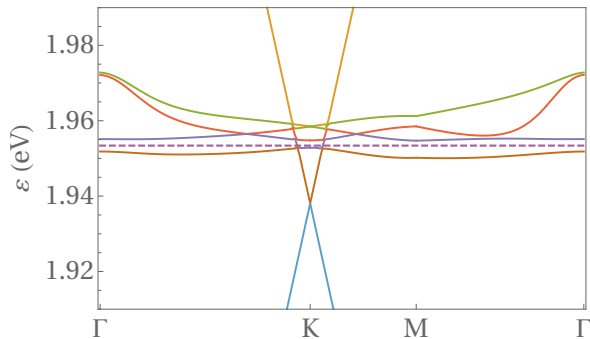


FIG. 3. Lowest valence and conduction bands of TtG at twist angle $\theta \approx 1.61^\circ$, computed in a self-consistent Hartree-Fock approximation with dielectric constant $\epsilon = 48$ and filling fraction of 2 holes per moiré unit cell (the dashed line stands for the Fermi level).

Hall density reset.— Experimentally, a reset from a large value down to zero Hall density is observed in TtG at 2-hole doping (as well as at 2-electron doping in the conduction side). In our interacting model, we can explain such a discontinuity as a result of the jump of the Fermi level across the gap shown in Fig. 3, from the bottom of the first VB to the top of the second VB.

As shown in the SM, in the semiclassical approximation, general closed trajectories usually lead to a universal Hall density $n_H = n$. Even extreme elliptic trajectories still fall under this universality class and anharmonic effects due to trigonal warping usually only lead to slight deviations. We thus start from a symmetric band model for each valence band where half of the band is dominated by electron transport and the other half by hole transport.

Non-universal behavior with $n_H \neq n$ only comes from open trajectories which are usually linked to vHSs.⁶¹ Around these points, the diverging Hall density is given by

$$n_H = \frac{n}{\pi} \ln \frac{\alpha \Lambda^2}{|\mu| + k_B T}, \quad (7)$$

where α is related to the inverse reduced mass, Λ the phenomenological band-cut-off and μ the relative chemical potential corresponding to the electronic density n . We also introduce the finite temperature T that smears out the logarithmic divergence which shall also include

disorder effects. Details on the derivation of Eq. (7) and the fitting procedure are given in the SM.

For a quantitative discussion of the Hall density in TtG, we consider the first and second VBs for $n = -1$ and $n = -2.8$, respectively, see SM. We expect deviations due to different filling factors to only slightly shift the energy of the vHS corrections. Due to the pronounced gap between the first and the second VB, there is a reset of the Hall density at $n = -2$ which leads to $n_H = n + 2$ for $n < -2$ due to the closed semi-classical orbits of the band structure near the band edge. For $n > -2$, the universal behavior is smeared out due to a van Hove singularity very close to the band edge, see SM. As mentioned above, the linear (universal) behavior is also obtained around filling factors $n = 0$ and $n = -4$.

Fig. 4 shows the Hall density n_H as function of the electronic density n for different temperatures $T = 0, 70$ mK, 1K. The energies and respective filling factors of the vHSs are indicated by the logarithmic divergence for $T = 0$, that are expected to change their position when the doping dependent band structure is taken into account. Also shown are the maximal values for each sub-band of the Hall density measured in Ref. 42 as well as the dashed purple lines indicating the universal behavior. The curve for $T = 1$ K agrees well with the experimental results performed at $T = 70$ mK which suggests a considerable amount of disorder in the unbiased sample.

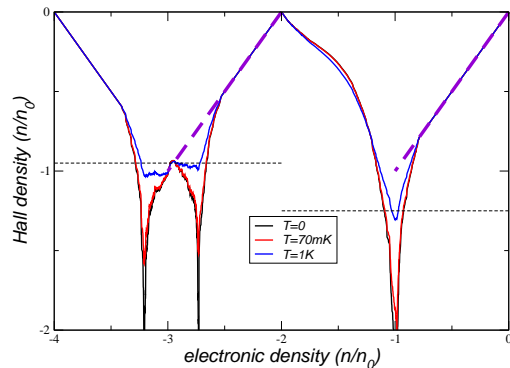


FIG. 4. Hall density as function of the filling factor in units of the density n_0 of one electron per moiré supercell for three different temperatures $T = 0, 70$ mK, 1 K. Also shown are the maximal values for each sub-band of the Hall density measured in Ref. 42 as well as the dashed purple lines indicating the universal behavior. The reset at $n = -2$ emerges due to the one-particle gap at the half-filled VB, see Fig. 3. The deviations from the universal behavior due to the presence of vHSs are described by Eq. (7).

Ising superconductivity.— The effect of VS breaking leads to Fermi lines for spin-up and spin-down electrons which are symmetric upon inversion of the momentum, as shown in Fig. 5. This opens the possibility of having Ising superconductivity, in which each spin projection in

a Cooper pair is attached to a different valley.^{53–55} The actual pairing instability takes place as a result of the anisotropy of the e - e scattering along the Fermi lines, which is strong enough to induce an effective attraction. This is characterized by the appearance of a negative coupling when projecting the Cooper pair vertex V onto the different harmonics along the Fermi line.

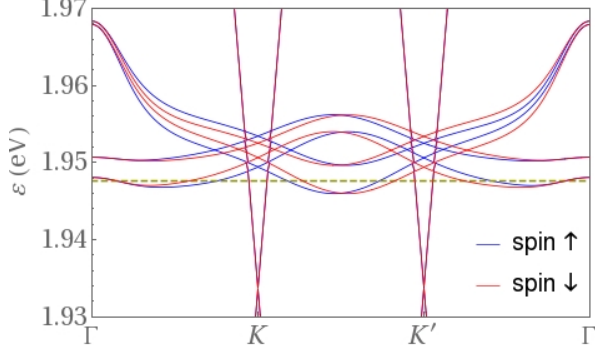


FIG. 5. Lowest-energy bands of TTB (computed for $\epsilon = 48$ and filling fraction $\nu = -2.4$) along a rectilinear path $\Gamma K K' \Gamma$, discerning the dispersion for spin-up and spin-down electrons.

The vertex V is indeed a function of the angles ϕ and ϕ' of the respective momenta of the spin-up incoming and outgoing electrons on each contour line of energy ϵ . The scattering of Cooper pairs in the particle-particle channel leads to a reduction of the amplitude of the vertex, given by the equation

$$V(\phi, \phi') = V_0(\phi, \phi') - \frac{1}{(2\pi)^2} \int_0^{\Lambda_0} \frac{d\epsilon}{\epsilon} \int_0^{2\pi} d\phi'' \frac{\partial k_{\perp}}{\partial \epsilon} \frac{\partial k_{\parallel}}{\partial \phi''} V_0(\phi, \phi'') V(\phi'', \phi') \quad (8)$$

where k_{\parallel}, k_{\perp} are the longitudinal and transverse components of the momentum for each energy contour line while $V_0(\phi, \phi')$ is the bare vertex at an energy cutoff Λ_0 . By differentiating Eq. (8) with respect to Λ_0 , we get

$$\epsilon \frac{\partial \hat{V}(\phi, \phi')}{\partial \epsilon} = \frac{1}{2\pi} \int_0^{2\pi} d\phi'' \hat{V}(\phi, \phi'') \hat{V}(\phi'', \phi') \quad (9)$$

with $\hat{V}(\phi, \phi') = F(\phi)F(\phi')V(\phi, \phi')$ and $F(\phi) = \sqrt{(\partial k_{\perp}/\partial \epsilon)(\partial k_{\parallel}/\partial \phi)/2\pi}$. Then, when there is a negative eigenvalue in the expansion of \hat{V} in harmonics, Eq. (9) leads to a divergent flow for that particular eigenvalue as $\epsilon \rightarrow 0$, which is the signature of the pairing instability.

The crucial point is the determination of $V_0(\phi, \phi')$ at the upper cutoff, for which one usually takes the interactions dressed at the scale Λ_0 . The relevant electron-hole processes can be summed up to give (see SM⁵⁸)

$$V_0(\phi, \phi') = \frac{v_{\mathbf{k}-\mathbf{k}'}}{1 + v_{\mathbf{k}-\mathbf{k}'} \chi_{\mathbf{k}-\mathbf{k}'}} + \frac{v_{\mathbf{Q}}^2 \chi_{\mathbf{k}+\mathbf{k}'}}{1 - v_{\mathbf{Q}} \chi_{\mathbf{k}+\mathbf{k}'}} \quad (10)$$

where \mathbf{k}, \mathbf{k}' are the respective momenta at angles ϕ, ϕ' and $\chi_{\mathbf{q}}$ is the particle-hole susceptibility at momentum transfer \mathbf{q} .

| Eigenvalue λ | harmonics | Irr. Rep. |
|----------------------|--------------------------------|-----------|
| 1.24 1.22 | $\{\cos(\phi), \sin(\phi)\}$ | E |
| 0.52 | $\sin(3\phi)$ | A_2 |
| 0.41 0.39 | $\{\cos(2\phi), \sin(2\phi)\}$ | E |
| -0.28 | $\cos(3\phi)$ | A_1 |
| -0.27 -0.27 | $\{\cos(4\phi), \sin(4\phi)\}$ | E |
| 0.21 0.21 | $\{\cos(5\phi), \sin(5\phi)\}$ | E |

TABLE I. Eigenvalues of the Cooper-pair vertex with largest magnitude (not including the constant mode) grouped according to the irreducible representations of the approximate C_{3v} symmetry, for filling fraction of 2.8 holes per moiré unit cell.

It now remains to expand the vertex V_0 in the different harmonics $\cos(n\phi), \sin(n\phi)$. We have carried out this analysis taking in particular the dispersion of the second VB shown in Fig. 2, for filling fraction $\nu = -2.8$. The results of the expansion can be grouped in terms of irreducible representations of the approximate symmetry C_{3v} , as shown in Table I. We observe that there is a dominant negative eigenvalue corresponding to the harmonic $\cos(3\phi)$ (with angles measured from one of the corners of the triangle-like Fermi lines in Fig. 2). From the resolution of Eq. (9), the negative eigenvalue λ leads to a pole at a critical energy scale (see SM⁵⁸)

$$\epsilon_c = \Lambda_0 e^{-1/|\lambda|} \quad (11)$$

This critical scale can be translated into the critical temperature T_c of the pairing instability. Taking for Λ_0 the bandwidth of the second VB shown in Fig. 2 (≈ 4 meV), we can estimate $T_c \sim 1$ K, which is consistent with the order of magnitude found in the experiments.

Finally, we can estimate the critical magnetic field that is needed to break up the Cooper pairs. For an in-plane field, orbital effects can be neglected and the Zeeman term will shift the energy of the spin up and spin down dispersions by $\pm \mu_B B$, respectively. When the dispersion of either valley becomes spin-degenerate, a spin-flip would lead to pair breaking. For an initial spin splitting $\Delta = 1.5$ meV, as seen in Fig. 5, the critical field is then given by $B_c = \Delta/2\mu_B \sim 13$ T, assuming the electron g -factor equal to 2. This scale has to be contrasted with the Clogston-Chandrasekhar or Pauli limit $B_p = 1.86 T_c$ (in Tesla for T_c in Kelvin).^{62,63} Even for $T_c \approx 3$ K, we thus find a violation of the Pauli limit by a factor 2-3, consistent with the experimental findings of Ref. 47. Let us finally note that the effective Zeeman splitting seen in the dispersion may arise from a chirality induced effective spin-orbit coupling.^{64,65}

Conclusion.— We have shown that the e - e interaction induces a strong breakdown of VS in TTB, with the two spin projections having opposite sign of the VS breaking order parameter. This leads to a spin-valley locking which has important implications for the superconductiv-

ity, explaining its protection against magnetic fields. VS breaking also implies a reduction of the symmetry from C_6 to C_3 , with an enhancement of the anisotropy of the bands which is at the origin of a Kohn-Luttinger (pairing) instability in the system. The isotropy of the bands is gradually recovered when the Fermi level approaches the bottom of the second valence band, explaining why superconductivity is lost beyond a certain doping in TTG.

VS breaking seems to be an ubiquitous feature in many moiré systems, and it is plausible that its role in the development of superconductivity may be also important in other derivatives of graphene. In this regard, it is remarkable that superconductivity has been recently found in rhombohedral trilayer graphene^{66–73}, which is another system close to an isospin instability. It would be perti-

nent then to reexamine the superconductivity of such systems in the light of VS breaking, including TBG, to confirm the connection between the enhanced anisotropy and the Kohn-Luttinger pairing instability established in this paper. Moreover, it should be interesting to confront preliminary results on twisted quadrilayer graphene, which make us expect an odd-even effect where the superconducting instability should be most protected in the central layer present for odd multilayers.

Acknowledgements. This work has been supported by MINECO (Spain) under Grant No. FIS2017-82260-P, MICINN (Spain) under Grant No. PID2020-113164GB-I00, as well as by the CSIC Research Platform on Quantum Technologies PTI-001. The access to computational resources of CESGA (Centro de Supercomputación de Galicia) is also gratefully acknowledged.

SUPPLEMENTAL MATERIAL

I. TIGHT-BINDING APPROACH AND HARTREE-FOCK APPROXIMATION FOR TWISTED TRILAYER GRAPHENE

We model twisted trilayer graphene in a tight-binding approach, taking as starting point the non-interacting Hamiltonian:

$$H_0 = - \sum_{\langle i,j \rangle} t_{\parallel}(\mathbf{r}_i - \mathbf{r}_j) (a_{i\sigma}^{\dagger} a_{j\sigma} + h.c.) - \sum_{(i,j)} t_{\perp}(\mathbf{r}_i - \mathbf{r}_j) (a_{i\sigma}^{\dagger} a_{j\sigma} + h.c.) , \quad (12)$$

The sum over the brackets $\langle \dots \rangle$ runs over pairs of atoms in the same layer, whereas the sum over the curved brackets (\dots) runs over pairs with atoms belonging to different layers (1 to 3). $t_{\parallel}(\mathbf{r})$ and $t_{\perp}(\mathbf{r})$ are hopping matrix elements which have an exponential decay with the distance $|\mathbf{r}|$ between carbon atoms. A common parametrization is based on the Slater-Koster formula for the transfer integral⁷⁴

$$-t(\mathbf{d}) = V_{pp\pi}(d) \left[1 - \left(\frac{\mathbf{d} \cdot \mathbf{e}_z}{d} \right)^2 \right] + V_{pp\sigma}(d) \left(\frac{\mathbf{d} \cdot \mathbf{e}_z}{d} \right)^2 \quad (13)$$

with

$$V_{pp\pi}(d) = V_{pp\pi}^0 \exp \left(-\frac{d - a_0}{r_0} \right) , V_{pp\sigma}(d) = V_{pp\sigma}^0 \exp \left(-\frac{d - d_0}{r_0} \right) , \quad (14)$$

where \mathbf{d} is the vector connecting the two sites, \mathbf{e}_z is the unit vector in the z -direction, a_0 is the C-C distance and d_0 is the distance between layers. A typical choice of parameters is given by $V_{pp\pi}^0 = -2.7$ eV, $V_{pp\sigma}^0 = 0.48$ eV and $r_0 = 0.319a_0$ ⁷⁴. In practice, we have taken these values to carry out the analysis reported in the main text, but restricting within each layer the hopping to nearest-neighbor atoms, as a way to get closer to the magic angle condition.

At the twist angles considered in the paper, the in-plane lattice relaxation of twisted trilayer graphene does not have the important role that it plays at the magic angle of the twisted bilayer. However, the out-of-plane corrugation of the trilayer is a relevant effect, which arises from the dependence of the interlayer interaction on the stacking of the graphene layers. Thus, the lattice structure tends to relax in the out-of-plane direction, reaching a minimum interlayer distance in the regions of AB stacking, and a maximum value in the regions of AA stacking. To describe the interlayer interaction we have used a Kolmogorov-Crespi potential^{75,76}

$$U(z) = -A \left(\frac{z_0}{z} \right)^6 + C e^{-\lambda(z-z_0)} \quad (15)$$

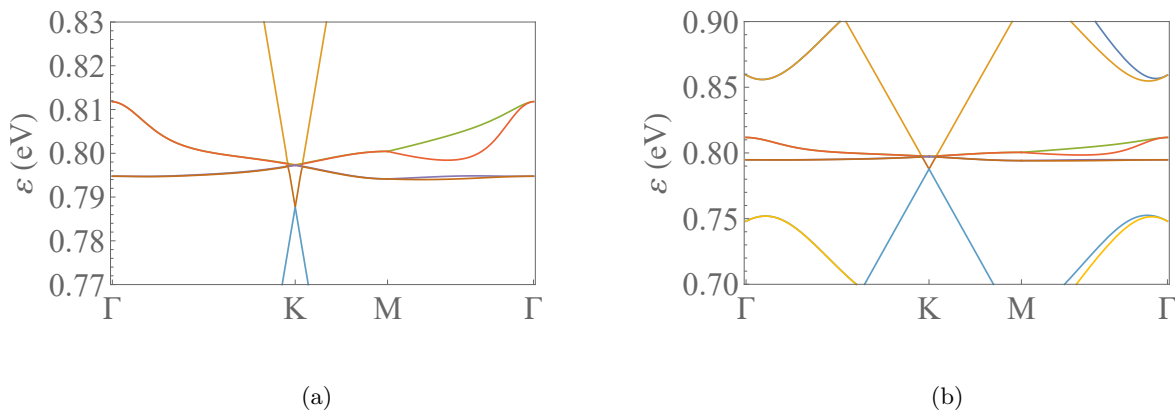


FIG. 6. Dispersion of the first valence and conduction bands (zoomed out in (b)) about the charge neutrality point of twisted trilayer graphene with twist angle $\theta \approx 1.61^\circ$, computed in a tight-binding approach with parameters given in the text.

where the first term stands for the van der Waals attraction and the second term accounts for an exponentially decaying repulsion due to the interlayer wave-function overlap. The effect of the registry of the carbon atoms is included in the second term, and we have adjusted it to interpolate between the different interaction energies in the regions of *AB* and *AA* stacking. In the relaxed structure we have left the central layer intact, so that the separation of the outer layers about the center becomes modulated across the superlattice according to the potential (15), reaching a minimum interlayer distance of 0.334 nm for *AB* stacking and a maximum distance of 0.356 nm for *AA* stacking.

Overall, our tight-binding approach leads to sensible results for the commensurate lattice studied in the main text with twist angle $\theta \approx 1.61^\circ$, whose first valence and conduction bands are shown in Fig. 6.

Turning to the *e-e* interaction, we have considered a form of the Coulomb potential which is adapted to the case where twisted trilayer graphene is surrounded by top and bottom metallic gates. The starting point is the unscreened Coulomb potential $v_0(\mathbf{r}) = e^2/4\pi\epsilon r$, ϵ being the dielectric constant of the surrounding (non-metallic) medium. In the presence of a gate at distance $z = \xi/2$, the electrostatic energy of two electrons lying in a plane parallel to the electric gate and being separated by a distance r is given by

$$v(\mathbf{r}) = \frac{e^2}{4\pi\epsilon} \left(\frac{1}{r} - \frac{1}{\sqrt{r^2 + \xi^2}} \right). \quad (16)$$

In the presence of an additional opposite gate also at distance $z = \xi/2$, and again using the image-charge technique, one obtains for the electrostatic energy

$$v(\mathbf{r}) = \frac{e^2}{4\pi\epsilon} \sum_{n=-\infty}^{\infty} \frac{(-1)^n}{\sqrt{r^2 + n^2\xi^2}} \quad (17)$$

$$= \frac{e^2}{4\pi\epsilon} \frac{2\sqrt{2}}{\xi} \frac{e^{-\pi r/\xi}}{\sqrt{r/\xi}}. \quad (18)$$

In the main text, we have addressed in particular the case of a setup with $\xi = 10$ nm.

When implementing the Hartree-Fock approximation, the construction of the self-energy in Eq. (4) of the main text demands the knowledge of the eigenvectors of the Hamiltonian. That self-energy implies a sum over the occupied states of the electronic bands, but in practice one has to impose some kind of truncation when carrying out the calculation. In this respect, we have retained the first 51 valence bands in the self-consistent resolution. Moreover, we have computed the self-energy taking a grid with 192 momenta (plus the Gamma point) covering the Brillouin zone. We have checked that such a content of filled states is safe to capture the relevant symmetry-breaking patterns of twisted trilayer graphene, as well as to obtain a sensible description of its low-energy bands.

II. INTERNAL SCREENING AND DIELECTRIC CONSTANT

An important question in the discussion of the electronic properties is the determination of the dielectric constant ϵ to be used for twisted trilayer graphene. The magnitude of that quantity depends mainly on the internal screening

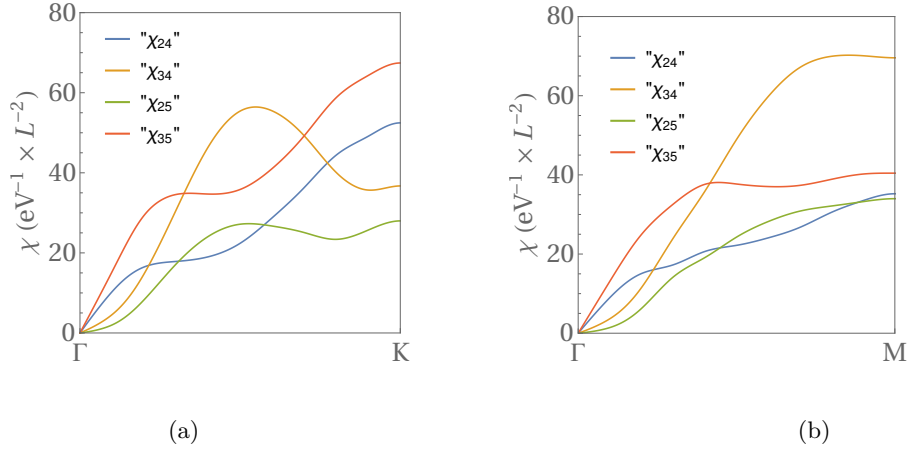


FIG. 7. Evolution along the ΓK (a) and the ΓM line (b) of the particle-hole susceptibility at the charge neutrality point of twisted trilayer graphene, computed in the model with the low-energy bands represented in Fig. 6. The plot shows the partial contributions between the two pairs of lowest-energy conduction ($i = 2, 3$) and valence ($j = 4, 5$) bands. The susceptibility is measured in units of $\text{eV}^{-1} \times L^{-2}$, where L is the lattice constant of the moiré superlattice.

of the Coulomb interaction, which becomes rather intense as a consequence of the reduced bandwidth of the lowest-energy valence and conduction bands. A good estimate of the dielectric constant can be obtained from the dielectric function $\epsilon(\mathbf{q}, \omega)$, which can be computed in the RPA for the two-dimensional Coulomb interaction as

$$\epsilon(\mathbf{q}, \omega) = 1 + \frac{e^2}{2\epsilon_0 |\mathbf{q}|} \chi(\mathbf{q}, \omega) \quad (19)$$

where $\chi(\mathbf{q}, \omega)$ stands for the particle-hole susceptibility. Since we are mainly interested in the screening of the interaction at length scales within the supercell of the twisted trilayer, we can estimate the magnitude of the dielectric constant from the values of the dielectric function $\epsilon(\mathbf{q}, 0)$ at large momenta \mathbf{q} , of the order of the inverse of the lattice constant of the superlattice.

The largest contributions to $\epsilon(\mathbf{q}, 0)$ come from the narrow bands shown in Fig. 6 near the charge neutrality point. We can approximate the susceptibility by considering particle-hole excitations between the two pairs of lowest-energy conduction ($i = 2, 3$) and valence ($j = 4, 5$) bands, which lead to the partial contributions shown as χ_{ij} in Fig. 7 along the two directions ΓK and ΓM . These susceptibilities are computed for the noninteracting bands displayed in Fig. 6, but they should provide anyhow a fair account of the screening in the interacting system, as far as this is dictated by the narrow dispersion of the low-energy bands.

We have for the dielectric function computed for instance at the large momentum \mathbf{Q}_K of the K point in the moiré Brillouin zone

$$\epsilon(\mathbf{Q}_K, 0) = 1 + \frac{e^2}{2\epsilon_0 |\mathbf{Q}_K|} \chi(\mathbf{Q}_K, 0) \quad (20)$$

$$= 1 + \frac{3}{8\pi\epsilon_0} e^2 L \chi(\mathbf{Q}_K, 0) \quad (21)$$

where L stands for the lattice constant of the moiré superlattice. We take $e^2/\epsilon_0 \approx 15.8 \text{ eV nm}$ and the length $L \approx 8.46 \text{ nm}$ appropriate for a twisted trilayer belonging to the commensurate sequence with $i = 20$. The particle-hole susceptibility can be obtained by adding the different contributions from Fig. 7 but paying attention to the fact that, in the valley symmetry breaking regime relevant for the paper, one of the valleys is pushed completely above the Fermi level, so that only one of the narrow valence bands contributes to the susceptibility. Having this in mind and accounting for the spin degeneracy, we get the estimate

$$\epsilon(\mathbf{Q}_K, 0) \sim 45 \quad (22)$$

Interestingly, we obtain a very similar magnitude if we carry out the estimate at the M point of the moiré Brillouin zone, taking again the values for the particle-hole susceptibility from the curves shown in Fig. 7. This confirms the validity of this method to determine the dielectric constant from internal screening. We also remark that the effect of screening from the dielectric environment can be included in the above computation, but making almost no

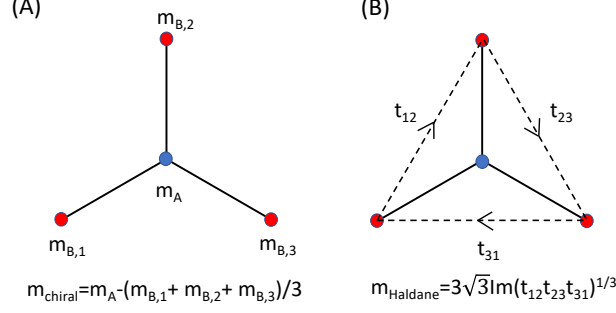


FIG. 8. Schematic definition of the two main symmetry breaking patterns opening a gap in the honeycomb lattice: (A) chiral symmetry breaking leading to a Dirac mass (where we have replaced h_{ii} defined in the text by m), (B) time-reversal symmetry breaking leading to the Haldane mass (where we have replaced h_{ij} defined in the text by t_{ij}).

difference in the final result, as long as the value of the dielectric constant in (22) is much larger than any typical dielectric constant ϵ_{env} of the substrate. That is, one can introduce ϵ_{env} in the above derivation, but this would reduce correspondingly the effect of the particle-hole susceptibility, leading to the cancellation of ϵ_{env} in the final expression for the effective Coulomb potential $e^2/2\epsilon|\mathbf{q}|$, with the value of ϵ already given by (22).

III. ORDER PARAMETERS AND PHASE DIAGRAM OF TWISTED TRILAYER GRAPHENE

In the self-consistent Hartree-Fock resolution, an important role is played by the matrix elements

$$h_{ij}^{(\sigma)} = \sum_a' \phi_{a\sigma}(\mathbf{r}_i) \phi_{a\sigma}(\mathbf{r}_j)^* . \quad (23)$$

where $\phi_{a\sigma}(\mathbf{r}_i)$ stand for the eigenvectors of the different states labeled by a and the spin σ , and depending on the atomic positions \mathbf{r}_i . The prime means that the sum is to be carried over the occupied levels. These matrix elements become also very useful in the definition of the order parameters for broken-symmetry phases. This is due to the fact that they coincide with the values of the equal-time propagator for the electron operators $a_{i\sigma}$. It can be actually shown that

$$\langle a_{j\sigma}^\dagger(t) a_{i\sigma}(t) \rangle = \sum_a' \phi_{a\sigma}(\mathbf{r}_i) \phi_{a\sigma}(\mathbf{r}_j)^* \quad (24)$$

This means that different charge densities as well as hopping parameters can be written in terms of $h_{ij}^{(\sigma)}$.

The main charge instability corresponds indeed to a mismatch in the charge densities for the two different sublattices A and B in each graphene layer. This leads to chiral symmetry breaking, with the opening of a gap between the low-energy Dirac cones at the charge neutrality point. Locally, the order parameter is given by the charge asymmetry between each carbon atom and its nearest neighbors, as represented in Fig. 8. Globally, the order parameter is defined by the quantity

$$C^{(\sigma)} = \sum_{i \in A} h_{ii}^{(\sigma)} - \sum_{i \in B} h_{ii}^{(\sigma)} \quad (25)$$

The other way to open a gap between the low-energy Dirac cones consists in producing an effective magnetic flux at each atomic site, which can be assessed by adding the phases of the hopping matrix elements between nearest neighbors i_1, i_2 and i_3 of each atom i , as represented in Fig. 8. The effective flux leads to time-reversal and parity symmetry breaking, conferring a so-called Haldane mass to the low-energy Dirac fermions. The order parameter for this broken-symmetry phase is given by

$$P_+^{(\sigma)} = \text{Im} \left(\sum_{i \in A} \left(h_{i_1 i_2}^{(\sigma)} h_{i_2 i_3}^{(\sigma)} h_{i_3 i_1}^{(\sigma)} \right)^{\frac{1}{3}} + \sum_{i \in B} \left(h_{i_1 i_2}^{(\sigma)} h_{i_2 i_3}^{(\sigma)} h_{i_3 i_1}^{(\sigma)} \right)^{\frac{1}{3}} \right) \quad (26)$$

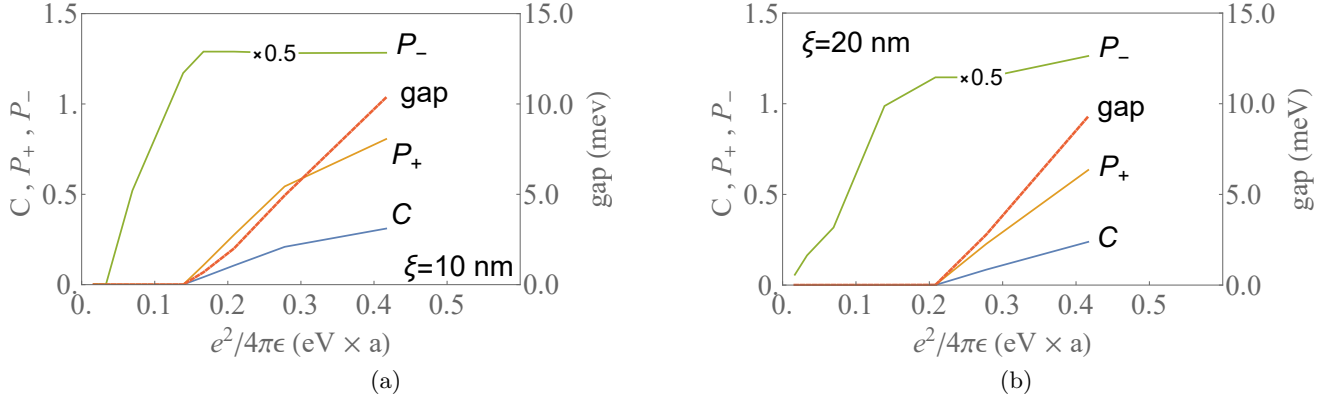


FIG. 9. Phase diagrams showing the different order parameters of symmetry breaking at a filling fraction of 2 holes per moiré unit cell in twisted trilayer graphene, obtained by means of the self-consistent Hartree-Fock approximation. The two instances correspond to screening length $\xi = 10$ nm (a) and 20 nm (b) for the extended Coulomb potential. The interaction strength is measured in units of eV times the C-C distance a .

where the nearest neighbors i_1, i_2 and i_3 are always taken with a definite orientation.

Furthermore, there is also the possibility of having an effective magnetic flux but preserving parity, which is realized by attaching opposite fluxes at atoms belonging to different sublattices A and B . The order parameter characterizing this phase is

$$P_-^{(\sigma)} = \text{Im} \left(\sum_{i \in A} \left(h_{i_1 i_2}^{(\sigma)} h_{i_2 i_3}^{(\sigma)} h_{i_3 i_1}^{(\sigma)} \right)^{\frac{1}{3}} - \sum_{i \in B} \left(h_{i_1 i_2}^{(\sigma)} h_{i_2 i_3}^{(\sigma)} h_{i_3 i_1}^{(\sigma)} \right)^{\frac{1}{3}} \right) \quad (27)$$

In the continuum theory of Dirac fermions, it can be shown that this breakdown of symmetry translates into the generation of a term proportional to the identity in pseudospin space. This does not open a gap in the Dirac cones at the K point, but the shift in the energy of the cones becomes different in the two valleys of the electron system. The main effect corresponds therefore to valley symmetry breaking, which is indeed an ubiquitous feature in graphene multilayers away from the charge neutrality point.

The evolution of the order parameters (25)-(27) can be studied as the strength of the extended Coulomb interaction is varied. The most interesting instance corresponds to a filling fraction of 2 holes per moiré unit cell. Then the dominant pattern of symmetry breaking corresponds to $P_-^{(\sigma)}$, while $P_+^{(\sigma)}$ and $C^{(\sigma)}$ open up beyond a certain interaction strength. This is illustrated in the phase diagrams shown in Fig. 9, which are the result of applying the self-consistent Hartree-Fock approximation for two different screening lengths $\xi = 10, 20$ nm. With our estimate of the dielectric constant (22), we have $e^2/4\pi\epsilon \approx 0.22 \text{ eV} \times a$ (where a is the C-C distance). This places the interaction in a regime where, apart from valley symmetry breaking, there is also a breakdown of time-reversal symmetry leading to a Chern insulator phase. The origin of this phase lies in the fact that, at the filling fraction of 2-hole doping, valley symmetry breaking sets the Fermi level at the vertices of the Dirac cones of the lower valley. The Dirac nodes may be destabilized then for a sufficiently strong interaction, mainly due to the appearance of the Haldane mass. This explains the opening of the gap at 2-hole doping, which is the relevant instance discussed in the main text.

IV. SEMICLASSICAL THEORY OF THE HALL DENSITY

In this Section, we will analyze the Hall density, accessible in typical transport experiments⁴². Within a semiclassical theory, electrons move on trajectories of constant energy. For small magnetic fields, these trajectory are not altered and we will thus use the energy contours of the flat-band dispersion obtained from the self-consistent Hartree-Fock calculations. For the first valence band, we use the filling factor $n = -1$, for the second valence band, we use the filling factor $n = -2.8$. In both cases, the dielectric constant is set to $\epsilon = 48$.

The contours can be divided into closed and open trajectories. Closed trajectories can be approximated by circular, elliptic or trigonal warped curves. Open trajectories shall be characterized by a van Hove singularities. In the following, we will obtain analytical formulas for all these situations.

A. Closed trajectories

For closed trajectories, we calculate the conductivity via the Chambers' formula

$$\sigma_{ij} = \frac{g_s g_v e^2}{(2\pi)^2} \int d^2 k v_i(\mathbf{k}) \int_{-\infty}^0 dt' v_j(\mathbf{k}(t')) e^{t'/\tau} \left(-\frac{\partial f(E)}{\partial E} \right). \quad (28)$$

By virtue of the Lorentz force rule, this can be transformed into the following expression:⁷⁷

$$\sigma_{ij} = \frac{g_s g_v}{(2\pi)^2} \frac{e^3 B}{\hbar^2} \int_0^T dt v_i(t) \int_{-\infty}^t dt' v_j(t') e^{(t'-t)/\tau} \quad (29)$$

The velocities $v_i(t)$ are obtained from the semiclassical equations,

$$\dot{\mathbf{r}} = \mathbf{v}(\mathbf{k}) = \frac{1}{\hbar} \partial_{\mathbf{k}} \epsilon_{\mathbf{k}}, \quad (30)$$

$$\dot{\mathbf{k}} = -\frac{e}{\hbar} [\mathbf{E} + \mathbf{v}(\mathbf{k}) \times \mathbf{B}]. \quad (31)$$

We assume the magnetic field perpendicular to the plane and the electric field in x -direction, i.e., $\mathbf{B} = B\mathbf{e}_z$ and $\mathbf{E} = E\mathbf{e}_x$. The equations of motion in the plane can be integrated and yield

$$\mathbf{r}(t) = -\frac{\hbar}{eB} \mathbf{e}_z \times \mathbf{k}(t) - \frac{E}{B} \mathbf{e}_y t. \quad (32)$$

The drift velocity $\mathbf{v}_D = -\frac{E}{B} \mathbf{e}_y$ is in fact the velocity of the frame of reference in which the electric field vanishes.⁷⁸ With $\tilde{\epsilon}_{\mathbf{k}} = \epsilon_{\mathbf{k}} - \hbar \mathbf{k} \cdot \mathbf{v}_D$, we can thus combine the equations of motion to the following compact form where only the magnetic field enters:

$$\dot{\mathbf{k}} = -\frac{e}{\hbar^2} \partial_{\mathbf{k}} \tilde{\epsilon}_{\mathbf{k}} \times \mathbf{B}, \quad (33)$$

In the following, we assume a small electric field and neglect the drift term.

Closed orbits are periodic in T and can thus be expanded into a Fourier series. We can therefore set

$$k_i(t) = \sum_{\nu} \kappa_{\nu}^i e^{i\nu\omega_c t}, \quad (34)$$

where we introduced the two components $i = x, y$ and the cyclotron frequency $\omega_c = 2\pi/T$. We now obtain the velocities $v_i(t)$ by differentiating Eq. (32) and with Chambers' formula, this finally yields

$$\sigma = \frac{g_s g_v}{2\pi} \frac{e^2 \tau}{m_c} \sum_{\nu > 0} \frac{\nu^2}{1 + (\nu\omega_c \tau)^2} \left(\frac{|\kappa_{\nu}^y|^2}{-\text{Re} [\kappa_{\nu}^x \kappa_{-\nu}^y (1 - i\nu\omega_c \tau)]} - \frac{\text{Re} [\kappa_{\nu}^x \kappa_{-\nu}^y (1 + i\nu\omega_c \tau)]}{|\kappa_{\nu}^x|^2} \right). \quad (35)$$

Since κ_{ν}^x is independent of B , this generally proves the Onsager relation $\sigma_{xy}(B) = \sigma_{yx}(-B)$. To be more explicit, we will now discuss isotropic and elliptic models.

1. Circular and elliptic curves

For the general isotropic dispersion $\epsilon_{\mathbf{k}} = \alpha |\mathbf{k}|^{\xi}$, the Fermi wave number is given by $k_F = (\mu/\alpha)^{1/\xi}$ with μ the chemical potential. This yields the circular trajectories $k_x(t) = k_F \cos(\omega_c t)$ and $k_y(t) = k_F \sin(\omega_c t)$ with the cyclotron frequency $\omega_c = \frac{eB}{m_c}$ and cyclotron mass $m_c = \frac{\hbar^2}{\xi\alpha} k_F^{2-\xi}$. Consistently, this is the same result as obtained from the general definition $m_c = \frac{\hbar^2}{2\pi} \frac{\partial A}{\partial \mu}$ with $A = \pi k_F^2$ denoting the area that is enclosed by the cyclotron orbit. With $(g_s g_v/4) k_F^2 = \pi n$, where g_s and g_v denote spin and valley (or other) degeneracies, this then gives the final result

$$\sigma = \frac{\sigma_{xx}}{1 + a^2} \begin{pmatrix} 1 & a \\ -a & 1 \end{pmatrix}, \quad (36)$$

where the longitudinal conductivity is given by $\sigma_{xx} = e^2 n \tau / m_c$ and $a = \omega_c \tau$. With the resistivity tensor $\rho = \sigma^{-1}$, we get for all isotropic dispersion relations the universal Hall density

$$n_H = - \left[e \frac{d\rho_{xy}}{dB} \right]^{-1} = n. \quad (37)$$

The universal result also holds for an elliptic dispersion with $\epsilon_{\mathbf{k}} = \alpha_x k_x^2 + \alpha_y k_y^2$ and $k_{F,i} = \sqrt{\mu/\alpha_i}$. With $k_x(t) = k_{F,x} \cos(\omega_c t)$, $k_y(t) = k_{F,y} \sin(\omega_c t)$, $A = \pi k_{F,x} k_{F,y}$ and $\omega_c = \frac{eB}{m_c}$, we have $m_c = \frac{\hbar^2}{2\sqrt{\alpha_x \alpha_y}}$ and

$$\sigma = \frac{\sigma_{xx}}{1 + a^2} \begin{pmatrix} \sqrt{\alpha_x/\alpha_y} & a \\ -a & \sqrt{\alpha_y/\alpha_x} \end{pmatrix}, \quad (38)$$

where $\sigma_{xx} = \frac{e^2 n \tau}{m_c}$. With Eq. (37), we again obtain the universal expression $n_H = n$ for the Hall density independent of the band parameters.

2. Trigonal warped trajectories

For trigonal warped Fermi-surfaces, there are deviations from the universal result. However, in a perturbative treatment the first non-vanishing term is quadratic in the expansion parameter $\epsilon \sim k_F a$. This suggests that general closed orbits will lead to a Hall density close to the universal result, i.e., $n = n_H$. This shall be discussed below.

To proceed analytically, let us discuss single-layer graphene in the trigonal warped regime. Graphene is characterized by the energy dispersion $\epsilon_{\mathbf{k}} = \pm t |\Phi_{\mathbf{k}}|$ where $\Phi_{\mathbf{k}} = \sum_{\delta} e^{i\mathbf{k} \cdot \delta}$ with the three nearest-neighbor vectors $\delta_1 = a(1, 0)$, $\delta_2 = a(-1/2, \sqrt{3}/2)$, and $\delta_3 = a(-1/2, -\sqrt{3}/2)$ as well as $t = -2.7$ the hopping matrix element. With the Jacobi-Anger expansion, the structure factor can also be written as $\Phi_{\mathbf{k}} = 3 \sum_n J_{-1+3n}(ka) e^{i(-1+3n)\phi}$. To lowest order in the lattice effect, we then have the following expression for the Fermi surface in polar coordinates:

$$k'_F(\phi) = k_F \left(1 + \epsilon \cos(3\phi) + \frac{\epsilon^2}{4} [11 + 5 \cos(6\phi)] \right) \quad (39)$$

The enclosed area is still given by $A = \pi k_F^2$ with $E_F = \hbar v_F k_F$ and $v_F = \frac{3}{2} a t$. We further introduced the trigonal warping parameter $\epsilon = \frac{k_F a}{4}$.

With $\mathbf{v} = -\frac{\hbar}{eB} \mathbf{e}_z \times \dot{\mathbf{k}}$, we have $\partial_{\mathbf{k}} \epsilon_{\mathbf{k}} = \frac{\hbar^2}{eB} [\dot{k} \phi \mathbf{e}_k - \dot{k} \mathbf{e}_\phi]$. With the dimensionless parameter $\bar{k} = k/k_F$, this gives the following set of differential equations:

$$\bar{k} \dot{\phi} = \omega_c \left[1 - 2\bar{k}\epsilon \cos(3\phi) - \frac{3}{4} (\bar{k}\epsilon)^2 [7 + \cos(6\phi)] \right] \quad (40)$$

$$\dot{\bar{k}} = -3\omega_c \bar{k} \epsilon \sin(3\phi) - \frac{3}{2} \omega_c (\bar{k}\epsilon)^2 \sin(6\phi) \quad (41)$$

To second order, the solution thus reads $\bar{k}(t) = 1 + \epsilon \cos(3\omega_c t) + \frac{\epsilon^2}{4} (17 - \cos(6\omega_c t))$ and $\phi(t) = \omega_c t - \epsilon \sin(3\omega_c t) + \epsilon^2 (-12\omega_c t + \frac{1}{2} \sin(6\omega_c t))$. For the cartesian coordinates, we then have $k_x(t) = k'_F(\phi(t)) \cos(\phi(t))$ and $k_y(t) = k'_F(\phi(t)) \sin(\phi(t))$. Note that for $k'_F(\phi(t))$ only the expansion of ϕ up to first order is needed in order to be consistent.

We can now again discuss the response in the presence of a magnetic field via the Chamber's formula. For the explicit solution of the trigonal warped graphene regime, we get

$$\sigma = \frac{e^2 n \tau}{m_c} \frac{1}{(1 + (\omega_c \tau)^2)(1 + 4(\omega_c \tau)^2)} \begin{pmatrix} 1 + 12\epsilon^2 + 4(1 + 9\epsilon^2)(\omega_c \tau)^2 & \omega_c \tau [1 + 4(1 + 6\epsilon^2)(\omega_c \tau)^2] \\ -\omega_c \tau [1 + 4(1 + 6\epsilon^2)(\omega_c \tau)^2] & 1 + 12\epsilon^2 + 4(1 + 9\epsilon^2)(\omega_c \tau)^2 \end{pmatrix}. \quad (42)$$

The Hall number is usually defined by

$$\frac{1}{n_H} = \frac{e}{B} \frac{\sigma_{xy}}{\sigma_{xx} \sigma_{yy} + \sigma_{xy}^2}. \quad (43)$$

This gives the final result

$$\frac{n_H}{n} = 1 + \left[6 + \frac{18}{1 + 4(\omega_c \tau)^2} \right] \epsilon^2. \quad (44)$$

In the clean limit $\tau \rightarrow \infty$, this simplifies to $n_H = n(1+6\epsilon^2)$ and in the low-field limit $\omega_c \rightarrow 0$, we have $n_H = n(1+24\epsilon^2)$. In both cases, there is thus a slight increase of the Hall number due to the acceleration around the corners of the deformed Brillouin zone.

The Hall number is also sometimes defined by

$$\frac{1}{n_H} = e \frac{d}{dB} \frac{\sigma_{xy}}{\sigma_{xx}\sigma_{yy} + \sigma_{xy}^2}. \quad (45)$$

This gives for the Hall density

$$\frac{n_H}{n} = 1 + \frac{24 [1 - (\omega_c \tau)^2 + 4(\omega_c \tau)^4]}{(1 + 4(\omega_c \tau)^2)^2} \epsilon^2, \quad (46)$$

which is a slightly different expression than above. However, in the clean limit, this again simplifies to $n_H = n(1+6\epsilon^2)$ and we also have $n_H = n(1+24\epsilon^2)$ for the low-field limit as before.

To conclude, there is no linear correction in ϵ to the Hall density. The deviations from the universal result $n_H = n$ should thus be small and negligible. We shall, therefore, approximate $n_H = n$ for all closed trajectories.

B. Trajectories close to van Hove singularities

To discuss the semiclassical motion of electrons close to a van Hove singularities, a well-defined regularization procedure is needed since the orbits are unbounded for a continuum theory. Therefore, we will not use the Chamber's formula, but start from the macroscopic equations of motion for the current density. The general response theory in the presence of an in-plane electric field \mathbf{E} and a perpendicular magnetic field \mathbf{B} then reads

$$\partial_t \mathbf{j} = \chi \mathbf{E} + \frac{e}{m_c} \bar{\mathbf{j}} \times \mathbf{B} - \mathbf{j} / \tau. \quad (47)$$

Above, we introduced the current-current response function χ in the dc-limit and the "average" current density $\bar{\mathbf{j}}$ which will both be discussed below. We also introduced the inverse relaxation time $\eta = \tau^{-1}$ and the cyclotron mass is defined by⁷⁸

$$m_c = \frac{\hbar^2}{2\pi} \frac{\partial A}{\partial \mu}, \quad (48)$$

where A denotes the area that is enclosed by the cyclotron orbit. Within this formalism, the above results for the isotropic and elliptic models can be obtained. Here, we will outline the specific case of a hyperbolic model.

1. Drude response around a saddle-point

The van Hove singularity shall be described by the saddle-point dispersion $\epsilon_{\mathbf{k}} = -\alpha_- k_x^2 + \alpha_+ k_y^2$. The so-called Drude response can entirely be obtained from the band structure and for $T = 0$ at the chemical potential μ , it is defined by

$$\chi_{ij} = \frac{g_s g_v e^2}{(2\pi \hbar)^2} \int d^2 k (\nabla \epsilon_{\mathbf{k}})_i (\nabla \epsilon_{\mathbf{k}})_j \delta(\mu - \epsilon_{\mathbf{k}}). \quad (49)$$

As we have assumed the principle axes to be along the x - and y -direction, $\chi_{ij} \propto \delta_{ij}$.

The above integral can be performed by first eliminating the δ -function via the polar integration. For the radial integration, the following integrals are needed:

$$\mathcal{I}_{\pm}(\Lambda, \gamma) = \int_1^{\Lambda^2} dx \sqrt{\frac{x-1}{\gamma x+1}}^{\pm 1} \quad (50)$$

This gives for $\mu = \pm|\mu|$ the final expression

$$\chi_{\pm} = \frac{g_s g_v e^2}{(2\pi)^2 \hbar^2} \frac{4\tilde{\mu}_{\pm}}{(\alpha_+ + \alpha_-)} \begin{pmatrix} \alpha_-^2 \mathcal{I}_{\pm}(\tilde{\Lambda}_{\pm}, \gamma_{\pm}) & 0 \\ 0 & \alpha_+^2 \mathcal{I}_{\mp}(\tilde{\Lambda}_{\pm}, \gamma_{\pm}) \end{pmatrix}, \quad (51)$$

with $\gamma_{\pm} = \alpha_{\mp}/\alpha_{\pm}$, $\tilde{\mu}_{\pm} = |\mu|/\alpha_{\pm}$, and $\tilde{\Lambda}_{\pm} = \Lambda/\sqrt{\mu_{\pm}}$ where Λ denotes the wavenumber cutoff. In the following, we will only discuss the response due to electron doping with $\mu > 0$ and set $\gamma = \gamma_{+}$.

At the neutrality point, the susceptibility is proportional to Λ^2 and we will discuss the difference $\delta\chi = \chi_{+} - \chi_{\mu=0}$. To leading order, we have

$$\delta\chi = \frac{g_s g_v}{(2\pi)^2} \frac{e^2}{\hbar^2} 2\mu \begin{pmatrix} -\sqrt{\gamma} \ln \frac{\alpha\Lambda^2}{\mu} & 0 \\ 0 & \sqrt{\gamma}^{-1} \ln \frac{\alpha\Lambda^2}{\mu} \end{pmatrix}, \quad (52)$$

where $\alpha = \frac{2\alpha_{+}\alpha_{-}}{\alpha_{+}+\alpha_{-}}$. The area relative to the one of $\mu = 0$ is given by $A = 4 \frac{\mu}{\sqrt{\alpha_{+}\alpha_{-}}} \ln \frac{4\alpha_{-}\Lambda^2}{\mu}$. Therefore, we get to leading order in Λ the cyclotron mass $m_c = 4 \frac{\hbar^2}{2\pi\sqrt{\alpha_{+}\alpha_{-}}} \ln \frac{4\alpha_{-}\Lambda^2}{\mu}$. With $n = \frac{g_s g_v}{(2\pi)^2} A$, this yields

$$\frac{m_c}{e^2} \delta\chi = \frac{n}{\pi} \begin{pmatrix} -\sqrt{\gamma} \ln \frac{\alpha\Lambda^2}{\mu} & 0 \\ 0 & \sqrt{\gamma}^{-1} \ln \frac{\alpha\Lambda^2}{\mu} \end{pmatrix}. \quad (53)$$

2. Magnetic response around a saddle-point

Let us now include the magnetic field. A magnetic field does not break rotational invariance and for an anisotropic system, the field couples to the average velocity $v^2 = v_x v_y$. For an elliptic dispersion, this yields the universal results $n_H = n$ as mentioned above.

In the case of a saddle-point, however, we also have to keep track of the negative sign and we have to couple to the positive mean velocity $v^2 = -v_x v_y$. From the cartesian velocities $v_i = \hbar^{-1} \partial_{k_i} \epsilon_{\mathbf{k}}$ and $\mathbf{j} = -en\mathbf{v}$, we thus set $\tilde{\mathbf{j}} = (j_x/\sqrt{\gamma}, -\sqrt{\gamma}j_y)$. The hyperbolic response with respect to $\mu = 0$ gives then rise to the following conductivity tensor:

$$\sigma = \frac{\tau}{1-a^2} \begin{pmatrix} \delta\chi_1 & -a\sqrt{\gamma}\delta\chi_2 \\ -a\delta\chi_1/\sqrt{\gamma} & \delta\chi_2 \end{pmatrix}, \quad (54)$$

where we used $\delta\chi = \text{diag}(\delta\chi_1, \delta\chi_2)$ of Eq. (52). The resistivity tensor thus reads

$$\rho = \frac{\eta}{\delta\chi_1 \delta\chi_2} \begin{pmatrix} \delta\chi_2 & a\sqrt{\gamma}\delta\chi_2 \\ a\delta\chi_1/\sqrt{\gamma} & \delta\chi_1 \end{pmatrix}. \quad (55)$$

Therefore, we get for the Hall density the final result

$$n_H = - \left[e \frac{d\rho_{xy}}{dB} \right]^{-1} = \frac{n}{\pi} \ln \frac{\alpha\Lambda^2}{\mu}. \quad (56)$$

There is a logarithmic divergence for $\mu \rightarrow 0$ which has been discussed also in the context of a tight-binding model.⁷⁷ However, for extended van Hove singularities there is also a possible divergence in the limit $\alpha \rightarrow 0$ which is independent of μ .

V. NUMERICAL DISCUSSION OF THE HALL DENSITY

In order to discuss the Hall density numerically, we start from a symmetric transport model, i.e., half of the band is dominated by electron transport and the other half by hole transport. This is justified by noting that close to the band edges, the trajectories are all closed. This "universal behavior" is, however, modified by the presence of two van Hove singularities which shall be modeled by Eq. (56). The expression for the Hall density around a van Hove singularity depends on the parameters α and Λ which shall now be determined.

Before we outlined the fitting procedure, let us recall we find a prominent valley symmetry breaking which reduces the inherent C_6 -symmetry to a C_3 -symmetry. This symmetry is also reflected in the van Hove singularities which are always composed of saddle-points that come in triplets. The positions of the van Hove singularities usually lie on the six ΓM -direction. Interesting, for the special case of filling factor $n = -2$, the two triplets lie on the same three ΓM -direction which enforces the valley-symmetry broken state.

Due to numerical errors, the C_3 -symmetry regarding the three-fold saddle points is not exact even though the appearance in the density plot suggests this approximate symmetry. We thus chose to fit the saddle point along the

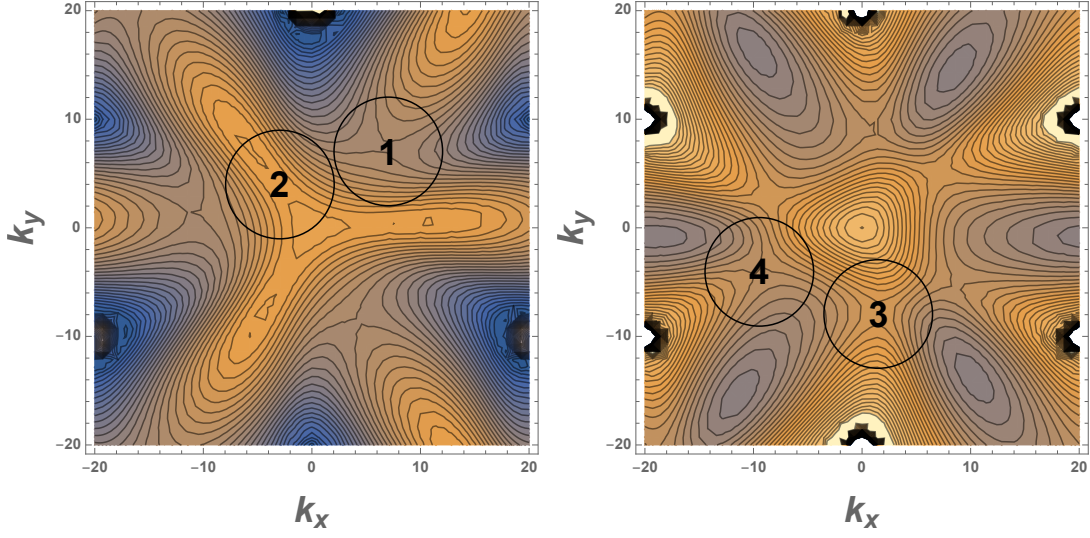


FIG. 10. Self-consistent energy dispersion of the first (left) and second (right) valence band for $n = -1$ and $n = -2.8$, respectively. The circles and numbers indicate the saddle points that are used for fitting the van Hove singularities. The wave numbers are in units of $\frac{1}{20} \frac{4\pi}{3a_M}$ with a_M the Moire lattice constant.

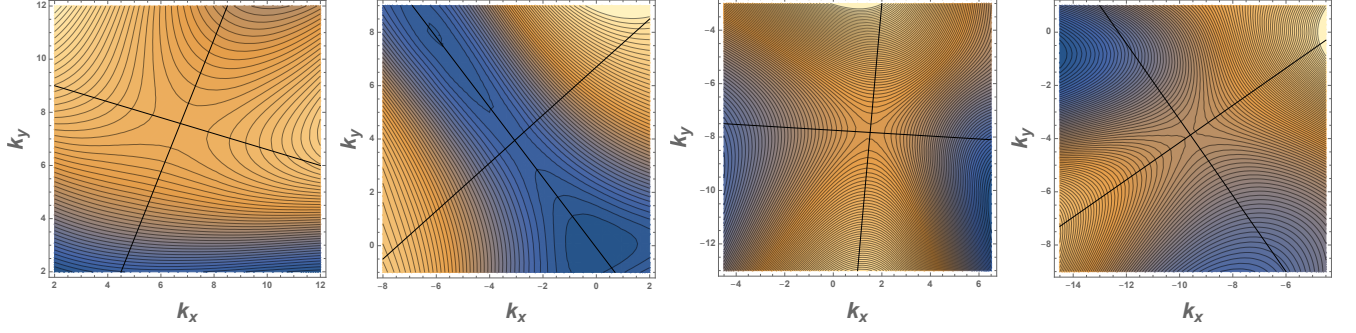


FIG. 11. Zoom-in of the van Hove singularities 1, 2, 3, 4 (from left to right). Also shown are the approximated principle axes along which the parameters of the saddle points are fitted. The wave numbers are in units of $\frac{1}{20} \frac{4\pi}{3a_M}$ with a_M the Moire lattice constant.

principle axis by the general dispersion $\epsilon_{\mathbf{k}} = -\alpha_- k_-^2 + \alpha_+ k_+^2$ which is closest to a parabola with positive and negative mass. In Fig. 10, we indicate and numerate the saddle points that were used in the fitting process. The initial discretization of the Brillouin zone was given by 20 k -points between the two K -points. With the moiré supercell lattice constant a_M , the wave numbers k_x and k_y are thus in units of $\frac{1}{20} \frac{4\pi}{3a_M}$.

We now fit the van Hove singularities along the principle axes as indicated in Fig. 11. Obviously, this procedure could be improved by considering curved trajectories, however, the overall result should hardly depend on it. By fitting the dispersion along the principle axes, there is also another scaling factor to be considered as we usually parametrize our curves by either k_x or k_y . The explicit comparison between the dispersion and the fitting result as function of these scaled wave numbers k_- and k_+ is shown in Fig. 12.

The results are listed in Table II.

What is left is the determination of the band-cut off Λ . This is done by demanding continuity with the universal regime $n_H = n$ at the cross-over chemical potential μ^* corresponding to the crossover density n^* :

$$\Lambda^2 = \frac{\mu^*}{\alpha} e^\pi \quad (57)$$

For the crossover density $|n^* - n_{vH}| = \Delta n$, we usually set $\Delta n = 0.2$. For the van Hove singularity 2 close to the band-edge, this has to be adjusted to $\Delta n = (2 - |n_{vH}|)/2$. For doping levels between two of the van Hove singularities, i.e., in the range $|n_{vH,1} - n_{vH,2}| - 2\Delta n$, we choose a linear interpolation of the two logarithmic singularities.

Finite temperature effects as well as possible disorder effects are included by substituting $|\mu| \rightarrow |\mu| + k_B T$ that smears out the logarithmic singularity. This makes the cutoff parameter dependent of the temperature and/or disorder. In

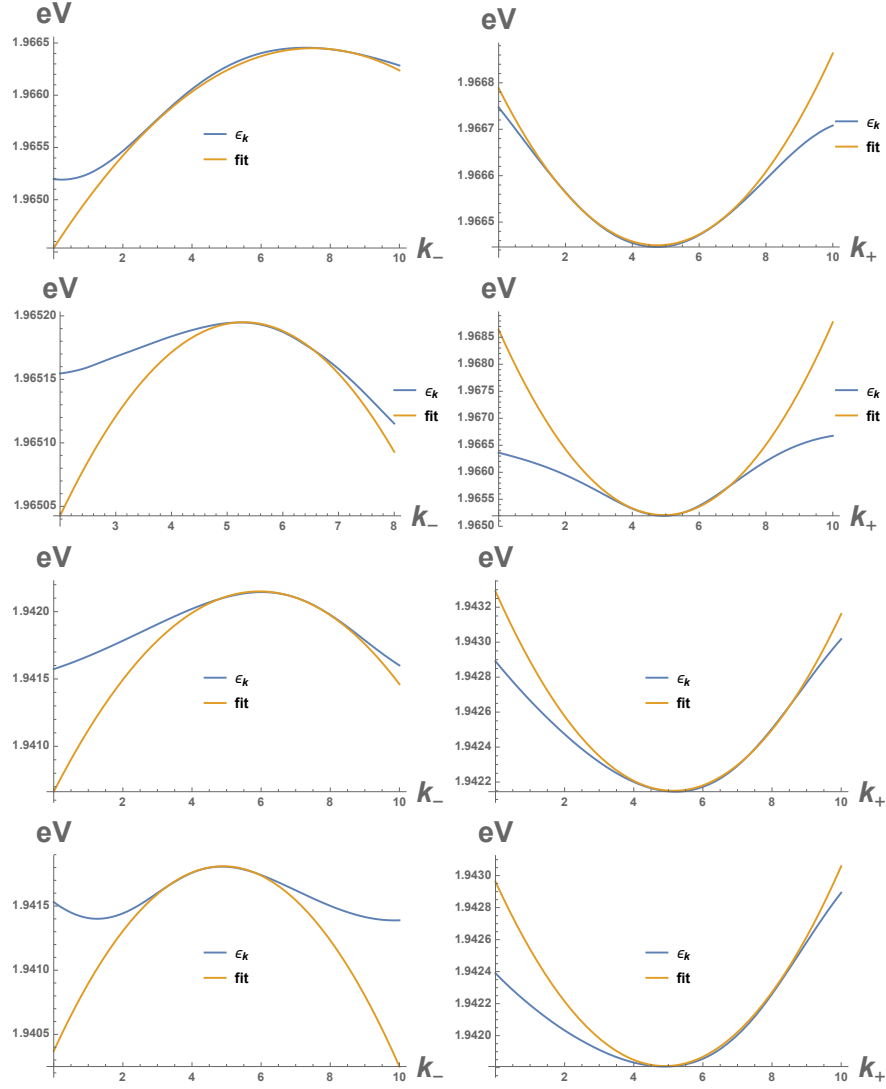


FIG. 12. Fitting results of the van Hove singularities 1, 2, 3, 4 (from top to bottom) for the negative (left) and positive (right) inverse mass.

Table II, we report the results for $T = 0, 70\text{mK}, 1\text{K}$. Let us note that $T = 70\text{mK}$ is the temperature used in the experiments of Ref. 42, however, we obtain the best fit for $T = 1\text{K}$ which suggests that there is considerable disorder in the sample without gate voltage.

Let us finally comment on the contribution of the Dirac cone that has been neglected in our analysis, so far. Due to mirror reflection symmetry, the flat bands and the Dirac cone decouple and can be treated separately. Dirac cones lead to circular trajectories due to their conical nature and thus again to universal behavior $n = n_H$ (assuming hole doping). However, the hole doping is only a fraction of the doping of the Moire supercell and can thus be safely neglected.

| i | ϵ_{vH} | n_{vH} | α_- | α_+ | α | Λ_{0K} | $\Lambda_{70\text{mK}}$ | Λ_{1K} |
|-----|-----------------|----------|------------|------------|----------|----------------|-------------------------|----------------|
| 1 | 1.9665 | -0.983 | 0.2470 | 0.0716 | 0.1110 | 4.26 | 4.38 | 7.02 |
| 2 | 1.9652 | -1.94 | 0.0424 | 0.3693 | 0.076 | 1.53 | 1.59 | 5.35 |
| 3 | 1.9422 | -2.73 | 0.1998 | 0.2032 | 0.2015 | 4.52 | 4.60 | 5.51 |
| 4 | 1.9418 | -3.21 | 0.1922 | 0.1538 | 0.1709 | 4.26 | 4.35 | 5.46 |

TABLE II. Energy of the van Hove singularities ϵ_{vH} (in eV), the corresponding filling number n_{vH} , and the fitting parameters α_{\pm} in units of $\text{meV} a_M^2$ defining the saddle point dispersion $\epsilon_k = -\alpha_- k_-^2 + \alpha_+ k_+^2$. We also list the scale that enters the expression of the Hall density, $\alpha = \frac{2\alpha_+ \alpha_-}{\alpha_+ + \alpha_-}$ (in $\text{meV} a_M^2$), and the band cutoff Λ_T (in a_M^{-1}) for $T = 0, 70\text{mK}, 1\text{K}$.

VI. PAIRING INSTABILITIES

Pairing instabilities can be studied by looking for singularities in the so-called BCS vertex, when incoming and outgoing electrons have total momentum equal to zero. For this purpose, we may collect the most divergent contributions in this channel, which leads to the iteration of particle-particle diagrams encoded in the diagrammatic equation shown in Fig. 13. The particle-particle loop at the right-hand-side of the equation involves an integration in momentum space, that can be parametrized in terms of the components k_{\parallel} and k_{\perp} which are parallel and normal, respectively, to the contour lines of constant energy. Alternatively, we can make a change of variables to the energy ε of the contour lines and the angle θ along them. Then, the self-consistent equation for the BCS vertex V becomes

$$V(\theta, \theta'; \omega) = V_0(\theta, \theta') - \frac{1}{(2\pi)^2} \int_0^\Lambda d\varepsilon \int_0^{2\pi} d\theta'' \frac{\partial k_{\perp}}{\partial \varepsilon} \frac{\partial k_{\parallel}}{\partial \theta''} V_0(\theta, \theta'') \frac{1}{\varepsilon - \omega} V(\theta'', \theta'; \omega) \quad (58)$$

where θ, θ' are the angles of the respective momenta of the spin-up incoming and outgoing electrons and ω is the sum of the frequencies of the modes in the pair.

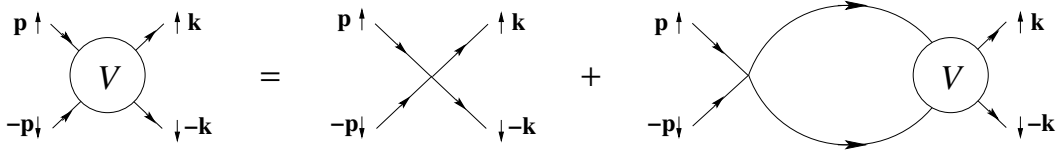


FIG. 13. Self-consistent diagrammatic equation for the BCS vertex V encoding the iteration of Cooper-pair scattering.

Eq. (58) can be cast in a more compact form by making the change of variables

$$\hat{V}(\theta, \theta'; \omega) = \sqrt{\frac{1}{2\pi} \frac{\partial k_{\perp}(\theta)}{\partial \varepsilon} \frac{\partial k_{\parallel}(\theta)}{\partial \theta}} \sqrt{\frac{1}{2\pi} \frac{\partial k_{\perp}(\theta')}{\partial \varepsilon} \frac{\partial k_{\parallel}(\theta')}{\partial \theta'}} V(\theta, \theta'; \omega) \quad (59)$$

After that, we can take the derivative with respect to the high-energy cutoff Λ and apply the self-consistency at the right-hand-side of the equation, to end up in the scaling equation

$$\Lambda \frac{\partial \hat{V}(\theta, \theta'; \omega)}{\partial \Lambda} = -\frac{1}{2\pi} \int_0^{2\pi} d\theta'' \hat{V}(\theta, \theta''; \omega) \hat{V}(\theta'', \theta'; \omega) \quad (60)$$

In Eq. (60) it is implicit that the BCS vertex must be actually a function of the ratio ω/Λ . Then, the scaling equation can be also used to find the behavior of the vertex in the low-energy limit $\omega \rightarrow 0$.

The analysis of Eq. (60) is facilitated by expanding the vertex in a set of orthogonal modes $\Psi_m^{(\gamma)}(\theta)$ corresponding to the different representations γ of the point symmetry group,

$$\hat{V}(\theta, \theta'; \omega) = \sum_{\gamma, m, n} V_{m,n}^{(\gamma)}(\omega) \Psi_m^{(\gamma)}(\theta) \Psi_n^{(\gamma)}(\theta') \quad (61)$$

We arrive then at the set of equations

$$\omega \frac{\partial V_{m,n}^{(\gamma)}}{\partial \omega} = \sum_s V_{m,s}^{(\gamma)} V_{s,n}^{(\gamma)} \quad (62)$$

where we have assumed that the vertex must depend on the combination ω/Λ .

In this framework, a pairing instability arises when any of the eigenvalues in the expansion (61) has a negative value $V^{(\gamma)}(\Lambda_0) < 0$ at the high-energy cutoff. Then, the solution of (62) leads to a divergent flow given by

$$V^{(\gamma)}(\omega) = \frac{V^{(\gamma)}(\Lambda_0)}{1 + V^{(\gamma)}(\Lambda_0) \log\left(\frac{\Lambda_0}{\omega}\right)} \quad (63)$$

In the flow towards the low-energy limit $\omega \rightarrow 0$, a singularity is reached at a critical frequency

$$\omega_c \approx \Lambda_0 \exp\{-1/|V^{(\gamma)}(\Lambda_0)|\} \quad (64)$$

which sets the scale of the superconducting instability.

In practice, one has to start with a sensible representation of the vertex $V(\theta, \theta')$ at the high-energy cutoff Λ_0 . This can be obtained by performing a sum of particle-hole contributions, building on the original diagrams which were considered in the seminal work by Kohn and Luttinger. Usually, one resorts to iterate in the particle-hole scattering shown in Figs. 14(a)-(b)⁸⁰. In our case, an important difference with respect to the discussion carried out for the Hubbard model is that the interaction is mediated by the extended Coulomb potential, as we are dealing with a manifold of atoms in the supercell of the moiré superlattice. Then, the sum of RPA and ladder contributions leads to an expression for the vertex

$$V(\theta, \theta'; \Lambda_0) = \frac{v(\mathbf{k} - \mathbf{k}')}{1 + v(\mathbf{k} - \mathbf{k}')\chi_{\text{ph}}(\mathbf{k} - \mathbf{k}')} + \frac{v^2(\mathbf{Q})\tilde{\chi}_{\text{ph}}(\mathbf{k} + \mathbf{k}')}{1 - v(\mathbf{Q})\tilde{\chi}_{\text{ph}}(\mathbf{k} + \mathbf{k}')} \quad (65)$$

where χ_{ph} ($\tilde{\chi}_{\text{ph}}$) stands for the susceptibility in the sum of bubble (ladder) diagrams. The interaction $v(\mathbf{Q})$ is a function of the momentum transfer \mathbf{Q} which depends on the sum of the momenta \mathbf{k}, \mathbf{k}' of incoming and outgoing electrons as well as on the momentum of the internal loop. In Eq. (65), the sum of RPA diagrams leads to screening of the interaction, making its contribution less relevant, while it is the sum of ladder diagrams encoded in the second term what may enhance potential pairing instabilities.

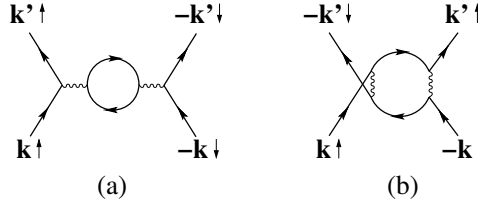


FIG. 14. Lowest-order diagrams contributing to the unrenormalized BCS vertex.

Once we compute the BCS vertex according to the expression in (65), the last stage of the analysis is the evaluation of the different coefficients in the expansion (61) at the high-energy cutoff. This can be easily made using the orthogonality of the modes, so that

$$V_{m,n}^{(\gamma)}(\Lambda_0) = \int_0^{2\pi} d\theta \int_0^{2\pi} d\theta' \hat{V}(\theta, \theta'; \Lambda_0) \Psi_m^{(\gamma)}(\theta) \Psi_n^{(\gamma)}(\theta') \quad (66)$$

This is the approach undertaken to determine the different eigenvalues for the BCS vertex in twisted trilayer graphene, applying in particular the convolution (66) with a large set of harmonics to capture the geometry of the energy contour lines shown in the main text for the second valence band.

-
- ¹ Y. Cao, V. Fatemi, A. Demir, S. Fang, S. L. Tomarken, J. Y. Luo, J. D. Sanchez-Yamagishi, K. Watanabe, T. Taniguchi, E. Kaxiras, R. C. Ashoori, and P. Jarillo-Herrero, *Nature* **556**, 80 EP (2018).
 - ² Y. Cao, V. Fatemi, S. Fang, K. Watanabe, T. Taniguchi, E. Kaxiras, and P. Jarillo-Herrero, *Nature* **556**, 43 EP (2018).
 - ³ M. Yankowitz, S. Chen, H. Polshyn, Y. Zhang, K. Watanabe, T. Taniguchi, D. Graf, A. F. Young, and C. R. Dean, *Science* **363**, 1059 (2019).
 - ⁴ E. Codecido, Q. Wang, R. Koester, S. Che, H. Tian, R. Lv, S. Tran, K. Watanabe, T. Taniguchi, F. Zhang, M. Bockrath, and C. N. Lau, *Science Advances* **5**, eaaw9770 (2019).
 - ⁵ C. Shen, Y. Chu, Q. Wu, N. Li, S. Wang, Y. Zhao, J. Tang, J. Liu, J. Tian, K. Watanabe, T. Taniguchi, R. Yang, Z. Y. Meng, D. Shi, O. V. Yazyev, and G. Zhang, *Nature Physics* **16**, 520 (2020).
 - ⁶ X. Lu, P. Stepanov, W. Yang, M. Xie, M. A. Aamir, I. Das, C. Urgell, K. Watanabe, T. Taniguchi, G. Zhang, A. Bachtold, A. H. MacDonald, and D. K. Efetov, *Nature* **574**, 653 (2019).
 - ⁷ G. Chen, A. L. Sharpe, P. Gallagher, I. T. Rosen, E. J. Fox, L. Jiang, B. Lyu, H. Li, K. Watanabe, T. Taniguchi, J. Jung, Z. Shi, D. Goldhaber-Gordon, Y. Zhang, and F. Wang, *Nature* **572**, 215 (2019).
 - ⁸ C. Xu and L. Balents, *Phys. Rev. Lett.* **121**, 087001 (2018).
 - ⁹ G. E. Volovik, *JETP Letters* **107**, 516 (2018).
 - ¹⁰ N. F. Q. Yuan and L. Fu, *Phys. Rev. B* **98**, 045103 (2018).
 - ¹¹ H. C. Po, L. Zou, T. Senthil, and A. Vishwanath, *Phys. Rev. B* **99**, 195455 (2019).
 - ¹² B. Roy and V. Jurivcić, *Phys. Rev. B* **99**, 121407 (2019).
 - ¹³ H. Guo, X. Zhu, S. Feng, and R. T. Scalettar, *Phys. Rev. B* **97**, 235453 (2018).

- ¹⁴ J. F. Dodaro, S. A. Kivelson, Y. Schattner, X. Q. Sun, and C. Wang, Phys. Rev. B **98**, 075154 (2018).
- ¹⁵ G. Baskaran, arXiv:1804.00627.
- ¹⁶ C.-C. Liu, L.-D. Zhang, W.-Q. Chen, and F. Yang, Phys. Rev. Lett. **121**, 217001 (2018).
- ¹⁷ K. Slagle and Y. B. Kim, SciPost Phys. **6**, 16 (2019).
- ¹⁸ T. J. Peltonen, R. Ojajärvi, and T. T. Heikkilä, Phys. Rev. B **98**, 220504 (2018).
- ¹⁹ D. M. Kennes, J. Lischner, and C. Karrasch, Phys. Rev. B **98**, 241407 (2018).
- ²⁰ M. Koshino, N. F. Q. Yuan, T. Koretsune, M. Ochi, K. Kuroki, and L. Fu, Phys. Rev. X **8**, 031087 (2018).
- ²¹ J. Kang and O. Vafek, Phys. Rev. X **8**, 031088 (2018).
- ²² H. Isobe, N. F. Q. Yuan, and L. Fu, Phys. Rev. X **8**, 041041 (2018).
- ²³ Y.-Z. You and A. Vishwanath, arXiv:1805.06867.
- ²⁴ F. Wu, A. H. MacDonald, and I. Martin, Phys. Rev. Lett. **121**, 257001 (2018).
- ²⁵ Y.-H. Zhang, D. Mao, Y. Cao, P. Jarillo-Herrero, and T. Senthil, Phys. Rev. B **99**, 075127 (2019).
- ²⁶ M. Ochi, M. Koshino, and K. Kuroki, Phys. Rev. B **98**, 081102 (2018).
- ²⁷ A. Thomson, S. Chatterjee, S. Sachdev, and M. S. Scheurer, Phys. Rev. B **98**, 075109 (2018).
- ²⁸ S. Carr, S. Fang, P. Jarillo-Herrero, and E. Kaxiras, Phys. Rev. B **98**, 085144 (2018).
- ²⁹ F. Guinea and N. R. Walet, Proceedings of the National Academy of Sciences **115**, 13174 (2018).
- ³⁰ L. Zou, H. C. Po, A. Vishwanath, and T. Senthil, Phys. Rev. B **98**, 085435 (2018).
- ³¹ E. Laksono, J. N. Leaw, A. Reaves, M. Singh, X. Wang, S. Adam, and X. Gu, Solid State Communications **282**, 38 (2018).
- ³² J. González and T. Stauber, Phys. Rev. Lett. **122**, 026801 (2019).
- ³³ J. Kang and O. Vafek, Phys. Rev. Lett. **122**, 246401 (2019).
- ³⁴ J. M. Pizarro, M. Rösner, R. Thomale, R. Valentí, and T. O. Wehling, Phys. Rev. B **100**, 161102 (2019).
- ³⁵ J. González and T. Stauber, Phys. Rev. Lett. **124**, 186801 (2020).
- ³⁶ Y. Choi, J. Kemmer, Y. Peng, A. Thomson, H. Arora, R. Polski, Y. Zhang, H. Ren, J. Alicea, G. Refael, F. von Oppen, K. Watanabe, T. Taniguchi, and S. Nadj-Perge, Nature Physics **15**, 1174 (2019).
- ³⁷ A. L. Sharpe, E. J. Fox, A. W. Barnard, J. Finney, K. Watanabe, T. Taniguchi, M. A. Kastner, and D. Goldhaber-Gordon, Science **365**, 605 (2019).
- ³⁸ S. Moriyama, Y. Morita, K. Komatsu, K. Endo, T. Iwasaki, S. Nakaharai, Y. Noguchi, Y. Wakayama, E. Watanabe, D. Tsuya, K. Watanabe, and T. Taniguchi, arXiv:1901.09356.
- ³⁹ Y. Jiang, X. Lai, K. Watanabe, T. Taniguchi, K. Haule, J. Mao, and E. Y. Andrei, Nature **573**, 91 (2019).
- ⁴⁰ Y. Xie, B. Lian, B. Jäck, X. Liu, C.-L. Chiu, K. Watanabe, T. Taniguchi, B. A. Bernevig, and A. Yazdani, Nature **572**, 101 (2019).
- ⁴¹ A. Kerelsky, L. J. McGilly, D. M. Kennes, L. Xian, M. Yankowitz, S. Chen, K. Watanabe, T. Taniguchi, J. Hone, C. Dean, A. Rubio, and A. N. Pasupathy, Nature **572**, 95 (2019).
- ⁴² J. M. Park, Y. Cao, K. Watanabe, T. Taniguchi, and P. Jarillo-Herrero, Nature **590**, 249 (2021).
- ⁴³ Z. Hao, A. M. Zimmerman, P. Ledwith, E. Khalaf, D. H. Najafabadi, K. Watanabe, T. Taniguchi, A. Vishwanath, and P. Kim, Science **371**, 1133 (2021).
- ⁴⁴ E. Khalaf, A. J. Kruchkov, G. Tarnopolsky, and A. Vishwanath, Phys. Rev. B **100**, 085109 (2019).
- ⁴⁵ S. Carr, C. Li, Z. Zhu, E. Kaxiras, S. Sachdev, and A. Kruchkov, Nano Letters **20**, 3030 (2020).
- ⁴⁶ A. Lopez-Bezanilla and J. L. Lado, Phys. Rev. Research **2**, 033357 (2020).
- ⁴⁷ Y. Cao, J. M. Park, K. Watanabe, T. Taniguchi, and P. Jarillo-Herrero, Nature **595**, 526 (2021).
- ⁴⁸ A. Fischer, Z. A. H. Goodwin, A. A. Mostofi, J. Lischner, D. M. Kennes, and L. Klebl, npj Quantum Materials **7**, 5 (2022).
- ⁴⁹ X. Liu, N. J. Zhang, K. Watanabe, T. Taniguchi, and J. I. A. Li, Nature Physics (2022).
- ⁵⁰ M. Christos, S. Sachdev, and M. S. Scheurer, arXiv:2106.02063.
- ⁵¹ J.-X. Lin, P. Siriviboon, H. D. Scammell, S. Liu, D. Rhodes, K. Watanabe, T. Taniguchi, J. Hone, M. S. Scheurer, and J. Li, arXiv:2112.07841.
- ⁵² H. D. Scammell, J. Li, and M. S. Scheurer, arXiv:2112.09115.
- ⁵³ J. M. Lu, O. Zheliuk, I. Leermakers, N. F. Q. Yuan, U. Zeitler, K. T. Law, and J. T. Ye, Science **350**, 1353 (2015), <https://www.science.org/doi/pdf/10.1126/science.aab2277>.
- ⁵⁴ Y. Saito, Y. Nakamura, M. S. Brahamy, Y. Kohama, J. Ye, Y. Kasahara, Y. Nakagawa, M. Onga, M. Tokunaga, T. Nojima, Y. Yanase, and Y. Iwasa, Nature Physics **12**, 144 (2016).
- ⁵⁵ X. Xi, Z. Wang, W. Zhao, J.-H. Park, K. T. Law, H. Berger, L. Forró, J. Shan, and K. F. Mak, Nature Physics **12**, 139 (2016).
- ⁵⁶ W. Kohn and J. M. Luttinger, Phys. Rev. Lett. **15**, 524 (1965).
- ⁵⁷ M. A. Baranov, A. V. Chubukov, and M. Yu. Kagan, International Journal of Modern Physics B **06**, 2471 (1992).
- ⁵⁸ See Supplemental Material for details of the tight-binding approach, the implementation of the Hartree-Fock approximation, the symmetry breaking order parameters, the derivation of the formulas for the Hall density, and the determination of the pairing instabilities.
- ⁵⁹ A. L. Fetter and J. D. Walecka, *Quantum Theory of Many-Particle Systems* (McGraw-Hill, New York, 1971).
- ⁶⁰ F. D. M. Haldane, Phys. Rev. Lett. **61**, 2015 (1988).
- ⁶¹ D. Guerci, P. Simon, and C. Mora, (2021), arXiv:2106.14911.
- ⁶² A. M. Clogston, Phys. Rev. Lett. **9**, 266 (1962).
- ⁶³ B. S. Chandrasekhar, Appl. Phys. Lett. **1**, 7 (1962).
- ⁶⁴ K. Yananose, G. Cantele, P. Lucignano, S.-W. Cheong, J. Yu, and A. Stroppa, Phys. Rev. B **104**, 075407 (2021).
- ⁶⁵ D. A. Bahamon, G. Gómez-Santos, and T. Stauber, Nanoscale **12**, 15383 (2020).

- ⁶⁶ H. Zhou, T. Xie, T. Taniguchi, K. Watanabe, and A. F. Young, *Nature* **598**, 434–438 (2021).
- ⁶⁷ Y.-Z. Chou, F. Wu, J. D. Sau, and S. Das Sarma, *Phys. Rev. Lett.* **127**, 187001 (2021).
- ⁶⁸ S. Chatterjee, T. Wang, E. Berg, and M. P. Zaletel, (2021), arXiv:2109.00002.
- ⁶⁹ A. Ghazaryan, T. Holder, M. Serbyn, and E. Berg, (2021), arXiv:2109.00011.
- ⁷⁰ Z. Dong and L. Levitov, (2021), arXiv:2109.01133.
- ⁷¹ T. Cea, P. A. Pantaleón, V. T. Phong, and F. Guinea, (2021), arXiv:2109.04345.
- ⁷² A. Szabo and B. Roy, (2021), arXiv:2109.04466.
- ⁷³ Y.-Z. You and A. Vishwanath, (2021), arXiv:2109.04669.
- ⁷⁴ P. Moon and M. Koshino, *Phys. Rev. B* **87**, 205404 (2013).
- ⁷⁵ A. N. Kolmogorov and V. H. Crespi, *Phys. Rev. Lett.* **85**, 4727 (2000).
- ⁷⁶ A. N. Kolmogorov and V. H. Crespi, *Phys. Rev. B* **71**, 235415 (2005).
- ⁷⁷ A. V. Maharaj, I. Esterlis, Y. Zhang, B. J. Ramshaw, and S. A. Kivelson, *Phys. Rev. B* **96**, 045132 (2017).
- ⁷⁸ N. W. Ashcroft and N. D. Mermin, *Solid State Physics* (Saunders College Publishing, 1976).
- ⁷⁹ G. Gómez-Santos and T. Stauber, *Phys. Rev. Lett.* **106**, 045504 (2011).
- ⁸⁰ D. J. Scalapino, E. Loh, and J. E. Hirsch, *Phys. Rev. B* **35**, 6694 (1987).